The diffusion induced stress and cracking behaviour of primary particle for Li-ion battery electrode

Xuanchen Zhu[1], Ying Chen[2], Haofeng Chen[1,2,*], Weiling Luan[2,*]

[1]*Department of Mechanical & Aerospace Engineering, University of Strathclyde, G1 1XJ, UK*

[2] *Key Laboratory of Pressure Systems and Safety (MOE), School of Mechanical and Power Engineering, East China University of Science and Technology, 200237, China*

Abstract

Mechanical fracture is commonly regarded as one of key ingredients affecting the reliability of Li-ion battery electrode. In order to avoid the rapid mechanical collapse of electrode, attempts have been made to work on obtaining the accurate critical fracture condition for electrode particle with initial cracks under diffusion-induced stress produced in Li-ion intercalation and deintercalation process. However, considering the integrated fracture process on pristine particle, it is crucial to assess crack initiation phase in fracture analysis so as to obtain the comprehensive failure margins of three-dimensional primary particle. This paper evaluates the diffusion induced stress for NCM primary particle morphology under lithiation-delithiation condition, where the coevolving process of diffusion and stress generation is implemented with both diffusion driven approach and chemical potential driven approach by developing finite element subroutines. Based on the coupled diffusion-stress analyses, crack onset and growth of ternary cathode particle are studied by using ABAQUS extended finite element method (XFEM) with appropriate mesh density and verified by experimental observation. The integrated crack initiation and fracture margins with various current densities and particle dimensions are plotted. The innovative equations to acquire critical particle dimension for crack initiation and fracture under applied electrochemical load are established, which are significant for evaluating particle status. Associating the critical failure diagram with the size distribution of particles in NCM electrode samples, the failure proportion is presented for electrode in microscale. The impact of diffusion on active material property is also investigated comprehensively in stress evolution and fracture analysis.

Keywords: Li-ion battery electrode, diffusion induced stress, crack initiation, crack propagation, critical margins

1. Introduction

As one of the most pivotal parts of Lithium-ion battery, electrode has driven many researchers to study and improve its operation efficiency and durability so as to fulfil the increasing usage demands from electric vehicles, portable electronic devices, etc. [1, 2, 3, 4]. Compared with traditional transition metal oxide cathode like $LiCoO_2$, ternary $LiNi_xCo_yMn_zO_2$ (NCM) has better electrochemical performance and relatively low material cost, which make it extensively used and researched in recent years as the rechargeable battery cathode [5, 6, 7]. On account of different synthesis approaches, there exists two categories of NCM microcosmic morphologies. One is spheroidal secondary particle structure composed of densely packed primary particles, and the other one is separated primary particle morphology with varying spheroid configuration [8]. In comparison with

* Corresponding author.
Email: haofeng.chen@strath.ac.uk (H Chen), luan@ecust.edu.cn (W Luan) Tel: +44(0) 141 548 2036

secondary particle structure, the primary particle NCM electrode exhibits relatively better mechanical stability under various measurement conditions, as the intergranular decohesion and fracture phenomenon between grains will result in serious mechanical degradation of secondary particles structure under electrochemical operation condition [9, 10]. However, the intragranular fracture behaviour is still a major factor affecting the mechanical stability and commercialization of NCM primary particle electrode [11].

During the process of Li-ion intercalating into and deintercalating from electrode particle, the inhomogeneous distribution of Li-ion concentration from kinetic limitation, together with solid state diffusion of Li-ions will generate evident diffusion induced stress (DIS) inside electrode particles, which further leads to fracture happened on particles and decline in the capacity of batteries [12, 13]. On the studying of stress arising from boron and phosphorus diffusing into silicon wafer, Prussin creatively calculated this type of stress by analogy to thermal stress [14]. Li [15] derived a series of analytical solutions for diffusion-induced stress in spherical, cylindrical, and thin plate structures. Christensen and Newman rose up a mathematical model to calculate concentration and stress profiles for the spherical electrode particle within lithiation and delithiation process, and further investigated the factors affecting the maximum stress, including charge rate, particle size and diffusivity [16]. Cheng and Verbrugge [17] have studied the development of diffusion-induced stress in spherical particles under potentiostatic and galvanostatic conditions by deriving analytical expressions. Korsunsky and co-workers [18] have established an expression for Li-ion concentration in a function of time and coordinate, and derived a closed form formulae for DIS in spherical particle. This work provides an efficient and effective basis for assessing the DIS caused damage of Li-ion battery components. Zhang and co-workers [19] systematically researched the intercalation-induced stress for $LiMn_2O_4$ electrode particles via finite difference method and finite element approach. The kinetic bidirectional effect between diffusion and mechanical stress has been investigated by Zhang [20] taking silicon as an example. Kalnaus and co-workers [21] investigated the diffusion-induced stress and fracture behaviour of Si particles during lithiation process, and verified the calculation results by acoustic emission test. Cui et al. [22] developed a stress-dependent chemical potential for solids under finite strain deformation and applied it to calculate the diffusion induced stress of silicon particle within lithiation-dilithiaion course with the consideration of both elastic and elastic-plastic conditions. A diffusion model with dimensionless equations is developed by Purkayastha et al. [23] and the influence of dimensionless current, maximum lithiation strain and partial molar volume on stress for spherical particles is clarified. For NCM ternary material, Wu et al. have employed the finite element method to analyse lithium intercalation stress on NCM three dimensional structures under various electrochemical conditions [24]. These research works present various numerical approaches to evaluate the DIS within spherical particle from different perspectives. Experimentally, multi-beam optical stress sensor [25], laser beam position detector [26], fiber optic sensor [27], etc. have all been used to determine the development of DIS in electrode material.

Based on the distribution of concentration and diffusion induced stress via performing the coupled electrochemical-mechanical investigation, it is more critical to explore the fracture behaviour of electrode particle so as to avoid life attenuation. Wolfenstine took the lead in concluding that the decreasing of particle size is beneficial for avoiding the occurrence of microcracks in electrode particle from the point of view of energy [28]. Aifantis [29] employed fracture mechanics to establish the stability diagrams considering crack growth for various microstructures of electrode material so as to seek for the most effective material configurations. Resorting to the linear elastic fracture mechanics, Hu and co-workers [30] employed critical energy release rate to decide the critical size of particle containing initial cracklike flaws so as to avert further cracking. In another work of this research group [31], by associating diffusion kinetics with

fracture mechanics, they established a fracture map according to non-dimensionalized discharge rate and elastic energy as the criterion for particle fracture. Yang [32] regarded the fracture as a pseudoreversible procedure and calculated the average size of fragments generated within lithiation process of spherical particle from energy viewpoint. Cheng and Verbrugge [33] worked out the analytical solution for total elastic energy in spherical particle caused by diffusion-induced stress. By further combining with Hasselman crack propagation model, they defined crack propagation criteria for spherical electrode. With the investigation on the growth of a pre-existing dominant flaw in single-particle electrode, Woodford [34] came up with the "electrochemical shock" map, which is plotted to relate the critical fracture C-rate with particle size under galvanostatic charging condition. Klinsmann and co-workers [35, 36] also developed a coupled model considering Li-ion diffusion, diffusion-induced stress and crack growth with the help of phase field method. The established model is applied to research the intragranular crack propagation and fracture of particles during lithiaiton-delithiation process. By applying the cohesive zone model in finite element analysis, Grantab [37] investigated the location and orientation dependent crack propagation behaviour in two-dimensional graphite particle model with pre-existing defects. Zhu et al. [38] employed the extended finite element method (XFEM) to study the effects of current density, particle size and particle aspect ratio on initial defect propagation in the $LiMn_2O_4$ cathode. The aforementioned investigations have employed different principles to study and avoid the fracture phenomenon of electrode material with pre-existing crack. While for pristinely primary electrode particle, the integrated fracture process include crack initiation, propagation and final fracture phase. Electrode material in different cracking status affects the electrochemical performance of battery to varying degrees. In addition, crack initiation and fracture generally follow different critical electrochemical excitation conditions. Therefore, it is significant that the fracture analysis of electrode particles is ought to assess the integrated crack initiation, evolution and fracture process. And the integrated critical failure boundary is required to be established so as to estimate the particle damage status under certain electrochemical load. In addition, the non-uniform particle size in micrometer scale decides the fact that the particles' dimension greater than the critical size will fracture under certain electrochemical load, while the rest particles remain stable. Hence, there is a need to associate the calculated critical particle dimension with the distribution of particle size in experimental samples.

In this present study, considering the complexity of subsequent cracking assessment, employing the analytical solutions of DIS to research the cracking of primary particle is not easily accessible. Hence, based on the finite element method, this work implements the diffusion driven approach and chemical potential driven approach to perform the coupled diffusion-stress analysis of NCM cathode particle via developing finite element user subroutines, which are for incorporating the coevolving process between diffusion and stress generation during intercalaction-deintercalaction condition. The calculation result difference between these two approaches is discussed. Based on the coupled diffusion-stress analysis, we apply ABAQUS XFEM to study the crack initiation, propagation and fracture of primary particle. Besides, critical crack initiation and fracture boundaries are established to avert the mechanical collapse of electrode. The equations to acquire critical particle dimension for crack onset and fracture under the applied electrochemical loads are fitted. The fracture proportion is proposed for battery electrode by associating the critical failure diagram with the size distribution of micro particles.

2. Computational Methods

Considering the stress induced fracture of cathode particles under coupled electrochemical-mechanical condition, essentially, the research emphasis can be classified as solving a coupled boundary value problem that is the coupled diffusion-mechanics issue, and conducting subsequent fracture evaluation. In this section, we provide the detailed formulas and methodologies for studying the diffusion process, mechanics simulation, fracture assessment in sequence, and further summarize the adopted material properties.

2.1. The first boundary value problem – diffusion equation

As for a heat conduction process, it obeys energy conservation law as listed below

$$\rho c_s \frac{\partial t}{\partial \tau} + \nabla q = \emptyset \tag{1}$$

Where ρ, c_s, t, $\emptyset$ denote density, specific heat, temperature and internal heat source respectively, and τ is defined as time here. The symbol q in the equation represents the heat flux, which describes the flow of energy per unit of area per unit of time.

When it comes to diffusion problem, Crank has solved basic equations in [39] where mass conservation law is satisfied:

$$\frac{\partial c}{\partial \tau} + \nabla J = 0 \tag{2}$$

Where c represents the concentration, and J is the diffusion flux which measures the amount of substance what will flow through a unit area during a unit time interval.

It is evident that one can make the following analogy so as to treat mass diffusion process as heat conduction process [37]

$$\begin{aligned} t&=c \qquad \emptyset = 0 \\ q&=J \qquad \rho c_s = 1 \end{aligned} \tag{3}$$

There are several approaches to update diffusion flux J so as to incorporate the bidirectional influence between stress and Li distribution. An effective method is the diffusion driven process based on classic Fick diffusion law. An alternative one stems from the chemical potential driven process.

For diffusion driven process [20], diffusion flux can be expressed as

$$J = -D\nabla c \tag{4}$$

$$D = D_0 \exp\left(\frac{\Omega \sigma_h}{RT}\right) \tag{5}$$

Where D is diffusivity, D_0 is diffusivity at stress-free condition, Ω represents the partial molar volume. σ_{h} is hydrostatic stress and can be calculated as $\sigma_{\mathrm{h}} = (\sigma_{11} + \sigma_{22} + \sigma_{33})/3$. The effect of stress on diffusion is incorporated in calculating diffusivity and diffusion flux, which are updated in real time based on the obtained hydrostatic stress at different instants. R is the gas constant, T denotes absolute temperature. The above equations can be implemented in ABAQUS by compiling a set of USDFLD-UMATHT subroutine to conduct diffusion driven coupled analysis.

For chemical potential driven process [19, 38], the diffusion process is driven by chemical potential gradient$\nabla\mu$, where the driven force F on particle can be determined by

$$F = -\nabla\mu \tag{6}$$

The minus sign in equation (6) represents that diffusion proceeds along the direction of decreasing chemical potential, and μ is the chemical potential which can be written as the following formula in ideal solid

$$\mu = \mu_0 + RT \ln X - \Omega\sigma_h \tag{7}$$

Where μ_0 is a constant and X is the molar fraction of lithium ion. The average diffusion velocity *v* of particle is in direct proportion of driven force *F*

$$v = MF = M(-\nabla\mu) \tag{8}$$

Where *M* is the mobility of solute. The diffusion flux in this method is then expressed as mass concentration of diffusion solute *c* timing its average velocity

$$J = cv = cM(-\nabla\mu) \tag{9}$$

By substituting equation (7) into equation (9), it is available to obtain another expression of diffusion flux with stress effect [38], as shown in equation (10). Resorting to the expression of chemical potential, the gradient of hydrostatic stress is embedded into calculating diffusion flux in real time.

$$J = -MRT\left(\nabla c - \frac{\Omega c}{RT}\nabla\sigma_h\right) \tag{10}$$

Through developing another set of USDFLD-UMATHT subroutine, the above formulas are accessible to be embedded in ABAQUS for performing coupled diffusion-stress analysis driven by chemical potential gradient. The main hinderance there is how to calculate the gradient of hydrostatic stress as it is not automatically past into UMATHT subroutine for information. In order to figure out this issue, we adopt a pointwise least squares linear regression method which was employed for calculating meaningful strain via obtained displacement in digital image correlation [40]. For obtaining the gradient of hydrostatic stress at one integration point, we assume coordinates and hydrostatic stress obey the following linear relationship within a sphere zone where the targeted integration point acts as the centre point of this sphere.

$$\sigma_h(x_i) = a_0 + a_1x_{1i} + a_2x_{2i} + a_3x_{3i} \quad (i = 1 \dots n) \tag{11}$$

Where a_0, a_1, a_2, a_3 are assumed polynomial coefficients needed to be fitted, $\sigma_h(x_i)$ represents the fitted value of hydrostatic stress based on the above linear relation. x_{1i}, x_{2i}, x_{3i} are coordinates of one integration and *n* represents all integration points within the sphere zone. Employing the least squares linear regression to minimize the fitting error.

$$e_i = y_i - \sigma_h(x_i) \tag{12-1}$$

$$S_r = \sum_{i=1}^{n} e_i^2 = \sum_{i=1}^{n}[y_i - (a_0 + a_1x_{1i} + a_2x_{2i} + a_3x_{3i})]^2 \tag{12-2}$$

Where y_i is the true value of the hydrostatic stress at each integration point and e_i is the difference between true value and fitted value of hydrostatic stress. If we partially differentiate S_r with each polynomial coefficient and equate it to zero

$$\frac{\partial S_r}{\partial a_0} = 0 = -2\sum_{i=1}^{n}[y_i - (a_0 + a_1x_{1i} + a_2x_{2i} + a_3x_{3i})] \tag{13-1}$$

$$\frac{\partial S_r}{\partial a_k} = 0 = -2\sum_{i=1}^{n}[x_{ki}(y_i - (a_0 + a_1x_{1i} + a_2x_{2i} + a_3x_{3i}))] \quad \text{(k=1, 2, 3)} \tag{13-2}$$

By reorganizing the equations we can obtain the following relations

$$a_0 n + a_1 \sum_{i=1}^{n} x_{1i} + a_2 \sum_{i=1}^{n} x_{2i} + a_3 \sum_{i=1}^{n} x_{3i} = \sum_{i=1}^{n} y_i \quad (14\text{-}1)$$

$$a_0 \sum_{i=1}^{n} x_{ki} + a_1 \sum_{i=1}^{n} x_{ki}\, x_{1i} + a_2 \sum_{i=1}^{n} x_{ki} x_{2i} + a_3 \sum_{i=1}^{n} x_{ki} x_{3i} = \sum_{i=1}^{n} x_{ki} y_i \text{ (k=1, 2, 3)} \quad (14\text{-}2)$$

Applying the hydrostatic stress and coordinates of all integration points in sphere zone to fit unknown polynomial coefficients, we will be accessible to calculate hydrostatic stress gradient of targeted integration point and further incorporate diffusion induced stress effect onto Li distribution.

The diffusion boundary condition in this paper is given as the Neumann boundary condition

$$J = \frac{i_n}{F_a} \quad (15)$$

Where i_n is the current density applied on the particles surface, F_a is Faraday constant.

2.2. The second boundary value problem – mechanics equation

For an elasticity issue, the equilibrium equation ignoring body forces F_{bj} and the geometric equation describing strain-displacement relation in elastomer can be given as equation 16 and 17 [19]

$$\sigma_{ij,i} = 0 \quad (16)$$

$$\varepsilon_{ij} = \frac{1}{2}(u_{i,j} + u_{j,i}) \quad (17)$$

The stress-strain relation considering thermal effect can be determined as following

$$\varepsilon_{ij} = \left(\frac{1+v}{E}\sigma_{ij} - \frac{v}{E}\sigma_{kk}\delta_{ij}\right) + \alpha \Delta T \delta_{ij} \quad (18)$$

Where ε_{ij}, σ_{ij} represent strain tensor and stress tensor respectively, E is elasticity modulus, v is Poisson's ratio, δ_{ij} is kronecher symbol, α is thermal expansion coefficient, ΔT is temperature increment. While, the constitutive equation under diffusion caused volumetric expansion situation is accessible to be written by

$$\varepsilon_{ij} = \left(\frac{1+v}{E}\sigma_{ij} - \frac{v}{E}\sigma_{kk}\delta_{ij}\right) + \frac{\Omega \Delta c}{3}\delta_{ij} \quad (19)$$

It is evident that we can make an analogy between these two constitutive equations as

$$\alpha \Delta T = \frac{\Omega \Delta c}{3} \quad (20)$$

Associating the above analogous term, ABAQUS coupled thermal-stress analysis could be converted to figure out targeted coupled diffusion-stress problem. With the consideration of a free-standing electrode particle surrounding by bonding material, the rigidity of bonding material is far less than electrode particle. We can assume that there is no traction at the particle surface. The mechanical boundary condition can then be set as traction-free surface for particle in this study [19] and expressed as

$$F_{sx} = \sigma_x l + \tau_{xy} m + \tau_{xz} n = 0 \quad (21\text{-}1)$$

$$F_{sy} = \tau_{yx} l + \sigma_y m + \tau_{yz} n = 0 \quad (21\text{-}2)$$

$$F_{sz} = \tau_{zx} l + \tau_{zy} m + \sigma_z n = 0 \quad (21\text{-}3)$$

Where l, m, n are direction cosines between axis and external normal.

2.3. Fracture assessment approach

Based on coupled diffusion-stress analysis, we subsequently employ Extended Finite Element Method (XFEM) in ABAQUS [41] to simulate the crack fracture and material damage of electrode particle. XFEM is applied for simulating the integrated cracking failure mechanism including crack onset and growth. As an extension of conventional finite element method, the conceptual framework of XFEM was presented by Belytschko and Black [42]. In XFEM, the asymptotic function near crack-tip is used to describe the stress singularity in crack tip area and the discontinuous function is induced to represent displacement jump crossing crack surfaces. XFEM is able to simulate crack initiation and propagation along an arbitrary path with no need to mesh for matching the geometry of the discontinuities or remesh near the crack [43]. In addition, XFEM can produce high precision numerical solution with sparse meshes. All these advantages make the XFEM to be an effective approach for solving discontinuity problem.

We hereby adopt the traction-separation damage model to describe the degradation and eventual failure of enriched elements. In this damage principle, the initial material response is assumed to be linear before damage initiation. When the stress or strain satisfies specific damage initiation criteria, the degradation begins accompanying with crack initiation. In our simulation, we induce the maximum principle stress criteria as the threshold for crack initiation, where damage occurs as the maximum principle stress exceeds material tensile strength. The following damage accumulation and crack propagation proceed in a simultaneous way, while the bearing capacity of enriched element declines with the crack growth. The eventual failure occurs when the critical fracture energy required is achieved and the element is going to be completed cracked.

2.4. Material property

All material parameters involved in this simulation work are summarized in Table 1. Where the material is assumed as isotropy due to the fact that microcosmic grains are distributed randomly. According to the statistical analysis on the size distribution of NCM cathode samples under micrometer scale, we simulate seven various particle diameters under a large range of current densities. Where the current density can be obtained as C-rate multiplied capacity, then divided by the area of electrode.

Table 1. Material properties

Property	Value
Particle diameter (um)	0.5, 0.7, 1, 2, 3, 4, 5
Constant average Young's modulus (GPa)	125 [44]
Poisson ratio	0.3 [44]
Maximum concentration (mol/m^3)	48230 [45]
Diffusivity (cm^2/s)	10^{-11} [45]
Partial molar volume (m^3/mol)	2.1E-6 [46]
Current density (A/m^2)	0.01-4
Damage initiation stress (MPa)	100[9]
Fracture energy (J/m^2)	0.11 [9]

3. Results and Discussion

3.1. Evaluation of diffusion induced stress

The evaluation of diffusion-induced stress works as the basis for failure analysis of electrode material. Due to the complexity of subsequent cracking assessment, the finite element method is

employed in this work to conduct the coupled diffusion-stress analysis by developing two subroutines, and the comparison validations of two approaches are performed. In addition, the effects of diffusion on the DIS are discussed.

Fig 1 (a) and (b) exhibit the distribution of von Mises stress along the radius of NCM primary particle under current density of 0.3, 1 A/m^2 with 125GPa Young's modulus during lithiation and delithiation phases respectively, where the couple effect between Li distribution and diffusion induced stress is implemented by diffusion driven method. Fig 1 (c) leaves the contours of Li-ion concentration at different moments within lithiation and delithiation stages, and Fig 1 (d) gives the corresponding contours of von Mises stress evolution process.

During the lithiation and delithiation process, the magnitudes of von Mises stress are positively related to the distance from particle centre at the most moments, where the maximum value takes place at the surface of primary particle. The exceptional case is at the initial phase of delithiation process, when the maximum von Mises stress happens at the interlayer of particle owing to the geometry configuration and conversion of diffusion direction. Besides, it is obvious to observe that higher current density will reduce the charging and discharging time, but generate greater stress profile and steeper stress gradient along radius, which ulteriorly bring more threat to the mechanical stability. Hence, it is significant to assess the critical current density so as to obtain the shortest charging-discharging time and maintain mechanical stability.

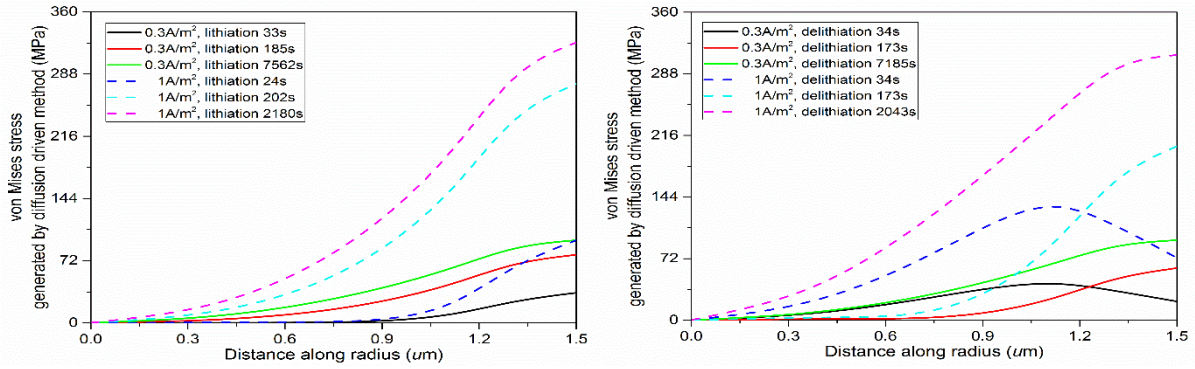

(a) (b)

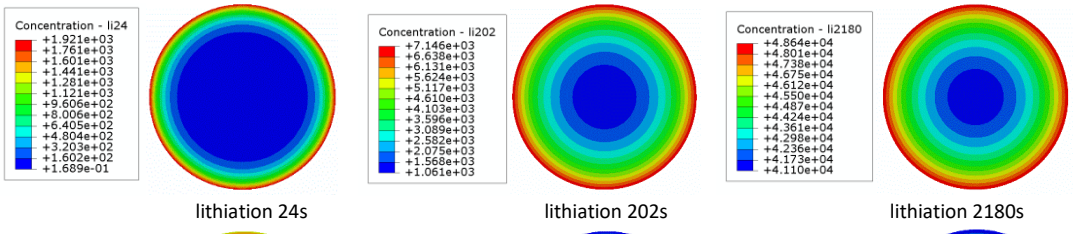

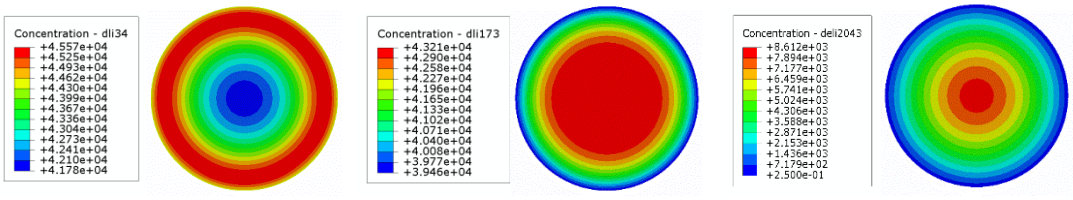

(c)

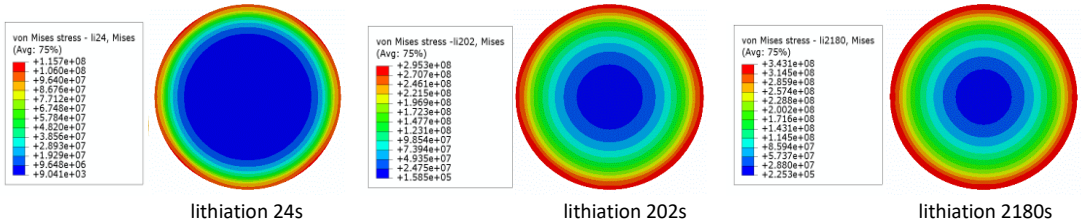

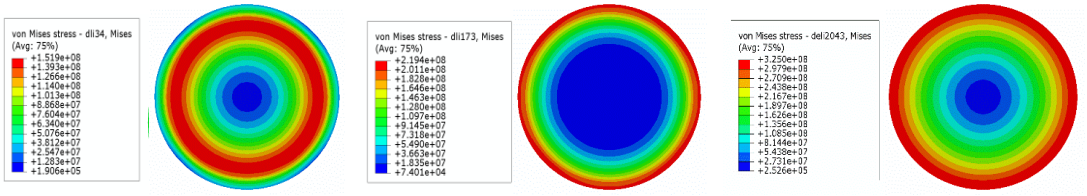

(d)

Fig 1 The evolution of von Mises stress produced by diffusion driven method for 3um diameter particle, stress distribution along radius during (a) lithiation process (b) delithiation process under 0.3A/m^2,1A/m^2 (c) contours of Li-ion concentration under 1A/m^2 at different moment (d) contours of von Mises stress under 1A/m^2 at different moments

Fig 2 shows the profile of maximum principle stress under the same simulation condition with von Mises stress. In comparison to von Mises stress, the maximum principle stress presents a negative correlation with the increase of distance to particle core at the lithiation phase. The core of particle always experiences the extremum of maximum principle stress, however the corresponding von Mises stress is zero. It is caused by the fact that the spherical geometry configuration makes the core of particle experience three same principle stress components. For the delithiation process, maximum principle stress at the centre of particle gradually converts from tensile stress to compressive stress owing to the variation of concentration gradient, while particle surface maintains tensile stress status during the overall deintercalation process. Considering the fact that the extremum of maximum principle stress in intercalation phase is greater than that of deintercalation phase and fracture only occurs under tensile stress, we can conclude that the core of particle is the most dangerous location under discharging-charging condition. Besides, the maximum principle stress field is worth more thinking when employing the maximum principle stress failure criterion in fracture analysis.

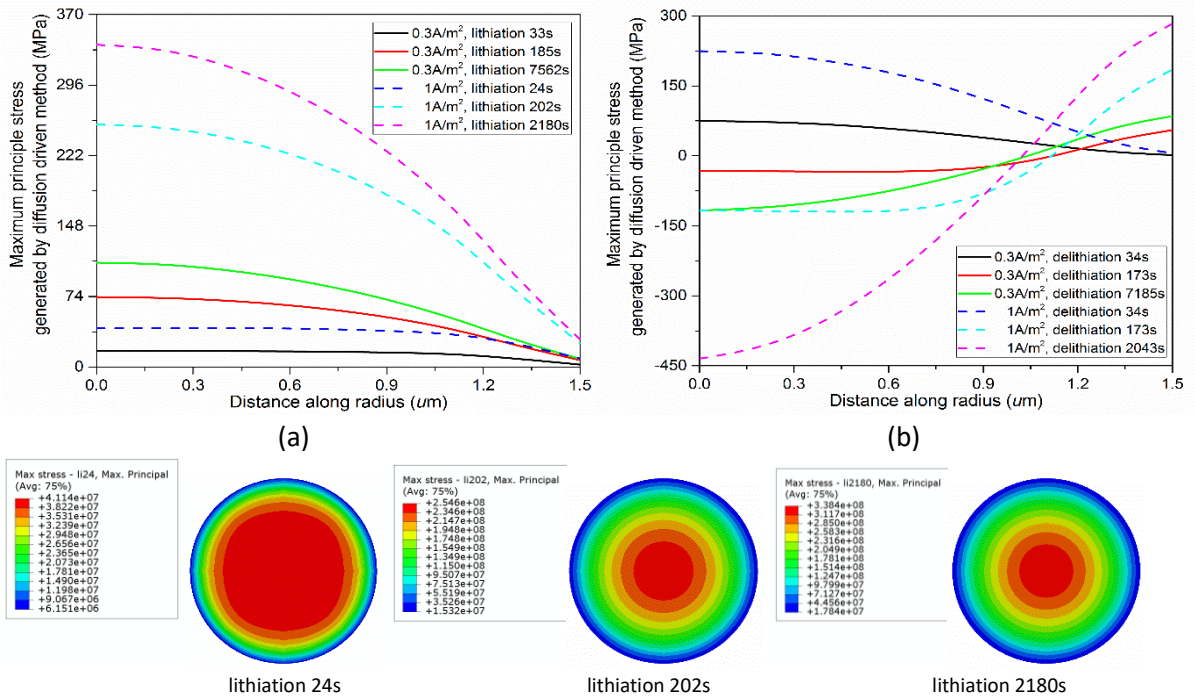

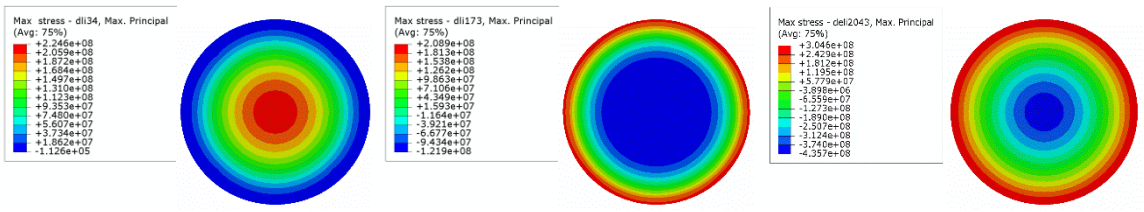

delithiation 34s delithiation 173s delithiation 2043s

(c)

Fig 2 The evolution of maximum principle stress produced by diffusion driven method for 3*u*m diameter particle, stress distribution along radius during (a) lithiation process (b) delithiation process under 0.3A/m^2,1A/m^2, (c) contours of maximum principle stress under 1A/m^2 at different moments

Based on the chemical potential driven principle, it is accessible to develop another set of ABAQUS subroutine for simulating the diffusion-induced stress and further make a comparison with the results produced from diffusion driven approach. Two sets of juxtaposition in Fig 3 exhibit the computed maximum principle stress from diffusion driven method and chemical potential driven method, where Fig 3 (a) shows the stress distribution along the radius of 3*u*m diameter particle with 125GPa Young's modulus under 0.3A/m^2 current density and Fig 3 (b) is for the same particle under 1A/m^2. It shows that, under relatively low current density condition (0.3A/m^2), two categories of couple diffusion-stress computation methods produce the proximate results. While under high current density level (1A/m^2), the calculation results represent significant differences on the centre of particle at the end phase of intercalation process and deintercalation process, where the differences reach 11.8% and -13.1% respectively.

The variance of simulation results lies on different ways to define diffusion flux so as to incorporate the bidirectional effect between diffusion and stress generation. For diffusion driven method, couple effect is incorporated in updating the diffusivity, while for the chemical potential driven method, the expression of chemical potential in the definition of diffusion flux implements this reciprocal influence. With the consideration of calculation efficiency, the chemical potential driven method costs more computing effort than the diffusion driven approach due to the requirement of distance judgement for every integration point with current calculating integration point at each iteration in ABAQUS subroutines. Hench, it is more efficient and also reliable to employ the diffusion driven approach to obtain the diffusion induced stress under relatively low current density condition.

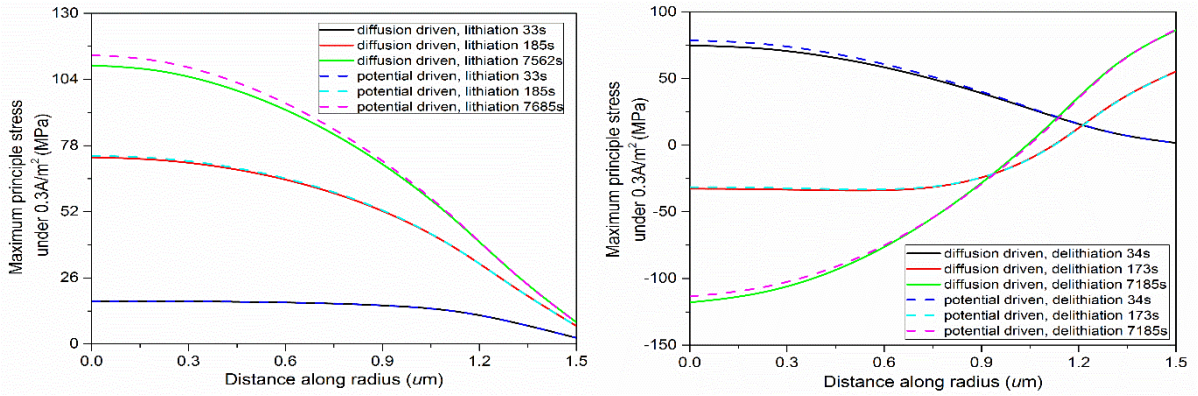

(a)

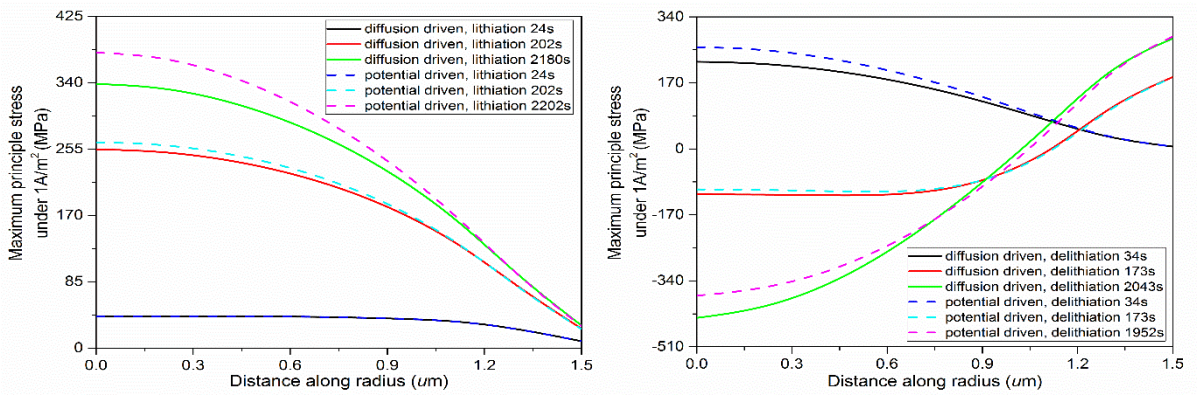

(b)

Fig 3 Comparison of diffusion induced stress profile generated by diffusion driven method and chemical potential driven method for 3*u*m diameter particle with 125GPa constant average Young's modulus (a) under 0.3A/m^2 current density (b) under 1A/m^2 current density

It is well known that the diffusion process will affect the material properties of active cathode. According to the experimental results [43], there exists a significant hardening phenomenon of NCM ternary material. The Young's Modulus of NCM523 cathode material will decline with the Li-ion deintercalation process owing to the decrease of bonding strength between transition metals ions and oxygen. It is shown that the Young's Modulus monotonically changes from 145GPa of $LiNi_{0.5}Co_{0.2}Mn_{0.3}O_2$ to 111GPa of $Li_{0.5}Ni_{0.5}Co_{0.2}Mn_{0.3}O_2$. Therefore, concentration dependent Young's Modulus should be considered as a key factor affecting the generation of diffusion induced stress. Fig 4 (a) shows the variational Young's Modulus for NCM523 cathode material with Li-ion concentration based on experimental data. Where 1 on the x-axis denotes $LiNi_{0.5}Co_{0.2}Mn_{0.3}O_2$ and 0.5 on the x-axis represents $Li_{0.5}Ni_{0.5}Co_{0.2}Mn_{0.3}O_2$. The Young's modulus can then be expressed as a function of concentration which is further determined by coordinates and time, $E = f[c(x,t)]$. For comparison calculation, constant average Young's modulus is still set as 125GPa during intercalation-deintercalation course.

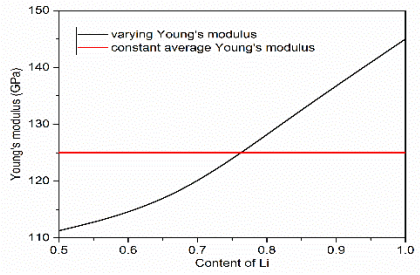

(a)

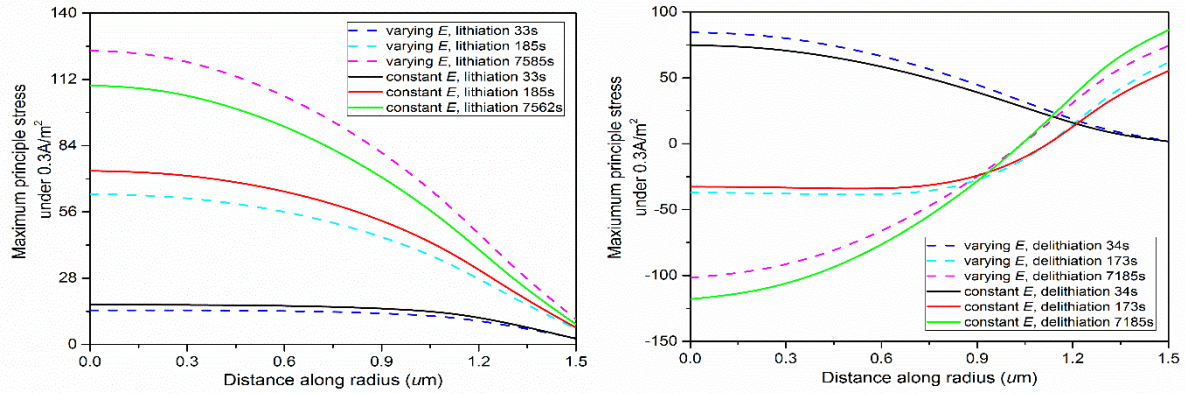

(b)

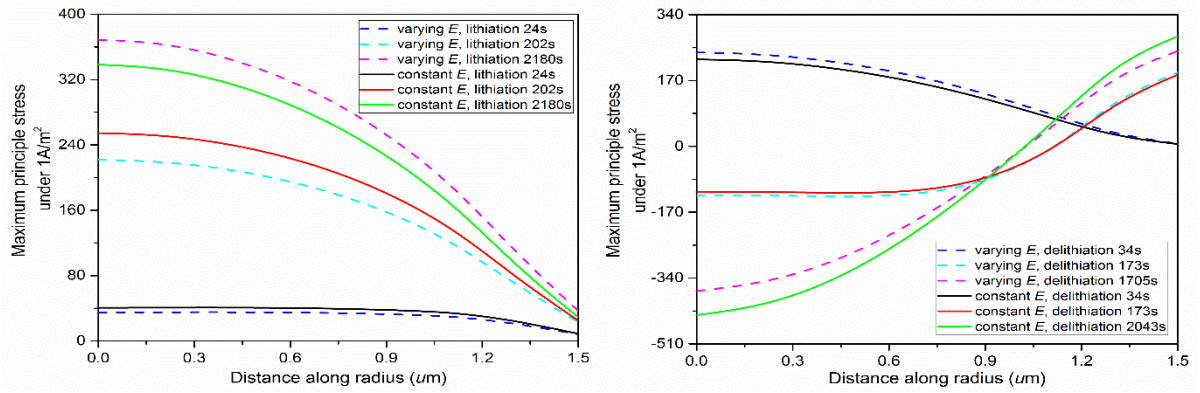

(c)

Fig 4 The effect of varying Young's modulus on maximum principle stress (a) the variation of Young's modulus with Li concentration (b) comparison of maximum principle stress with varying Young's modulus and constant Young's modulus of particle under 0.3A/m^2 during lithiation-delithiation phases (c) comparison of maximum principle stress with varying Young's modulus and constant Young's modulus of particle under 1A/m^2 during lithiation-delithiation phases

Fig 4 (b) makes a comparison of maximum principle stress with concentration dependent Young's modulus and constant Young's modulus under 0.3A/m^2 during lithiation and delithiation phases, and Fig 4 (c) gives the comparison for maximum principle stress under 1A/m^2. It can be observed that concentration dependent Young's modulus has an obvious impact on diffusion induced stress evolution process. On the whole, stress evolution trends under 0.3A/m^2 and 1A/m^2 are almost analogous. Apparently, at the initial phase of lithiaiton course and the end phase of delithiation course, the maximum principle stress generated with constant Young's modulus is greater than that of concentration dependent Young's modulus. Conversely, at the relatively deep li-imbedding stage including the end phase of lithiation course and the initial phase of delithiation course, maximum principle stress with varying Young's modulus exceeds that of constant average Young's modulus. It is due to the fact that the maximum principle stress is in direct proportion to the magnitude of Young's modulus which is positively determined by Li-ion concentration. Associating with the fact that cracking fracture is always caused by tensile stress, it can be concluded that the changing Young's modulus caused by Li-ion concentration variation will aggravate the fracture at the particle centre within lithiation phase, but is beneficial for avoiding fracture at particle surface during delithiation stage.

3.2. Fracture evaluation

3.2.1. Crack initiation

The cracking behaviour of cathode material under DIS will expose fresh surfaces of active materials to the electrolyte and influence the stability of the battery. In addition, the cathode material under different electrochemical loads will be in different cracking stages which affect battery performance to varying degrees. Hence, this work conducts the integrated cracking assessment form initiation to fracture, and studies the critical triggering conditions for various cracking status. Based on the coupled diffusion-stress analysis, we employ ABAQUS extended Finite Element Method (XFEM) to study the mechanical fracture mechanism of NCM primary particle. Where the material degradation and crack initiation happen when the maximum principle stress within enriched element reaches the damage initiation stress.

In the ideal state, the spherically symmetrical geometry model, boundary conditions and uniform material property will generate spherically symmetrical stress field distributed like the above stress calculation results. Associating the maximum principle stress failure criteria with the maximum principle stress distribution of the particle shown in Fig 2, crack and damage will initiate

from the particle centre. Nevertheless, the lack of stress concentration point around the particle centre will lead to the result that crack cannot grow along specific direction after initiation. Fig 5 (a) exhibits the damage distribution of 3um particle under $0.2875A/m^2$ with spherically symmetric stress field. Where the variable STATUSXFEM presents the status of enriched element, and it varies from 0 (non-damage status) to 1 (completely cracked). It can be observed that the damage initiates at the centre of particle, but there is no existing of crack in the centre zone. Fig 5 (b) presents the TXM tomogram of individual NCM particle after charging at C/3 rate [47]. Where the relation between C-rate and current density is based on the parameter characteristics of practically tested Li-ion battery. In our experiments, the capacity of coin cell is 0.1mAh. Under this case, the corresponding current density for C/3 is $0.294A/m^2$. From TXM tomogram, it can be seen that the practical crack initiates from the centre of particle and gradually propagates outward along specific direction. In reality, this is due to the fact that the practical particles cannot be perfectly spherical, and the material is not absolutely uniform. Therefore, the practical diffusion induced stress field cannot be spherically symmetrical within the particle.

In the finite element analysis, establishing irregular geometry model, adopting non-uniform material property, applying an additional stress disturbance can all be employed to simulate this non-uniform stress field. In this work, for equivalently studying the crack behaviour under the non-uniform stress field, we add a tiny stress disturbance on the model. A concentrated force, which is far less than the diffusion induced stress, is applied to an arbitrary point on the particle surface so as to simulate the non-perfectly spherically symmetrical stress in practice, as given in Fig 6 (a). Fig 6 (b) shows the contour of non-uniform maximum principle stress for 3um particle under $0.2875A/m^2$ with considering the stress disturbance. From which we can observe that the integral stress distribution is spherically symmetrical except the finite area around the point applied the concentrated force. Under this circumstances, the integral stress status is not changed, but the introduction of the tiny stress disturbance applied on the arbitrary direction makes it accessible for crack to propagate.

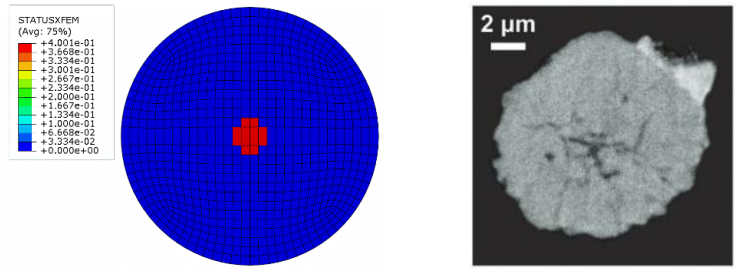

(a) (b)

Fig 5 (a) Damage distribution of 3um particle under $0.2875A/m^2$ with spherically symmetric stress field, (b) TXM tomogram of individual NCM particle after charging at C/3 rate to 4.5V [47]

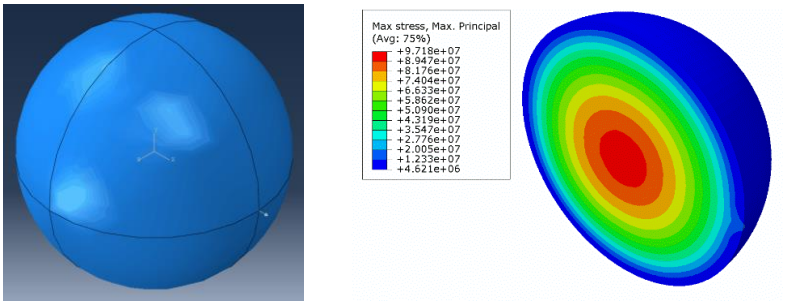

(a) (b)

Fig 6 (a) Particle model with a tiny stress disturbance acting on one arbitrary point of the surface, (b) The maximum principle stress distribution for 3um particle under $0.2875A/m^2$ considering stress disturbance

In addition, the appropriate mesh density is required to be defined in cracking simulations, as the mesh sensitivity is commonly regarded as a significant factor affecting crack initiation status. Fig 7 presents the obtained critical current density on crack initiation under different mesh densities for 3um diameter particle. Obviously, the decreasing of element size is beneficial to obtain more accurate stress field. But the calculation results show that the obtained critical current density keeps constant when the element size is less than 0.16. From the point of view of computational efficiency, the element size of 0.14 is set for the subsequent cracking analyses.

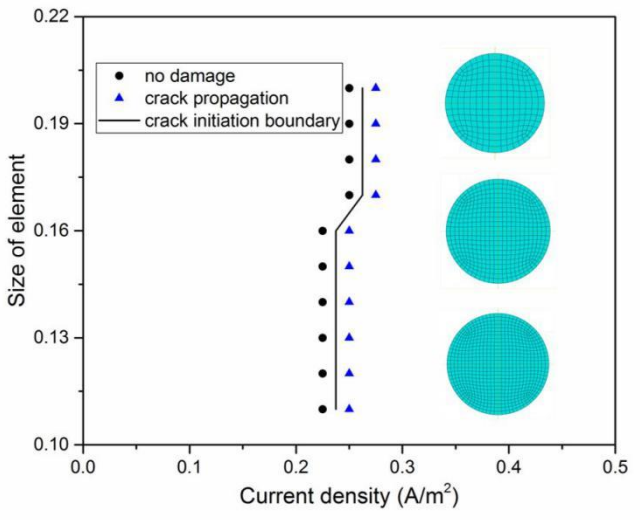

Fig 7. The critical current density of crack initiation for 3um particle under different mesh densities.

We subsequently perform the crack initiation analysis of NCM individual particle under diffusion induced stress field with a stress disturbance. Fig 8 (a) plots the critical current density for crack initiation against varying particle size. Where the diffusion driven approach is applied for conducting coupled diffusion-stress analysis and the effect of diffusion on Young's modulus is incorporated. In Fig 8 (a), blue diamond and light blue five-pointed star represent the permissible current density for corresponding particle size without crack initiation, red dot and magenta pentagen indicate superfluous current density leading to cracking. Apparently, in both cases, the permissible current density for primary particle increases with the decline of particle size, and reducing the average size of particles is beneficial for improving the mechanical stability for NCM electrode. Fig 8 (b), (c) exhibit the distribution of crack and status of enriched elements for NCM single particle with concentration-dependent Young's modulus under no-damage current density ($0.225A/m^2$) and damage current density ($0.2875A/m^2$). Under no-damage current density, the entire particle

maintains stable status. While for the damage current density, crack initiates at the core of particle which has been verified from TXM tomogram of NCM particle after charging in Fig 5 (b) [47].

In addition, Fig 8 (a) presents that the effect of diffusion on material mechanical property will weaken the electrochemical bearing capacity of NCM cathode material. For a specific particle size, the permissible current density with concentration dependent Young's modulus is lower than that with constant average Young's modulus. The result is due to the combined effect of stress generation process and maximum principle stress failure criterion. According to the evaluation of diffusion induced stress, the extremum of tensile maximum principle stress always occurs at the end stage of lithiation process on the particle core, when the concentration dependent Young's modulus has exceeded the constant average Young's modulus on account of high Li-ion concentration. In this case, particle core with concentration dependent Young's modulus will experience relatively greater tensile maximum principle stress under the same current density comparing with the particle holding constant average Young's modulus. Hence, for NCM ternary cathode material under a specific maximum principle stress failure criterion, incorporating the concentration dependent Young's modulus will produce a relatively conservative crack initiation boundary than employing the assumed constant average Young's modulus, and it is crucial to incorporate this diffusion effect on Young's modulus so as to obtain the accurate critical condition in the following fracture analysis. In view of particle at 3*u*m diameter, degradation and crack will occur under relatively low current density condition. According to comparative stress calculation analysis from the previous section, in this case, diffusion driven approach and chemical potential driven method produce almost the same stress field. Therefore, for improving calculation efficiency, the diffusion driven approach will be employed to perform the coupled diffusion-stress analysis as the input condition for subsequent fracture evaluation.

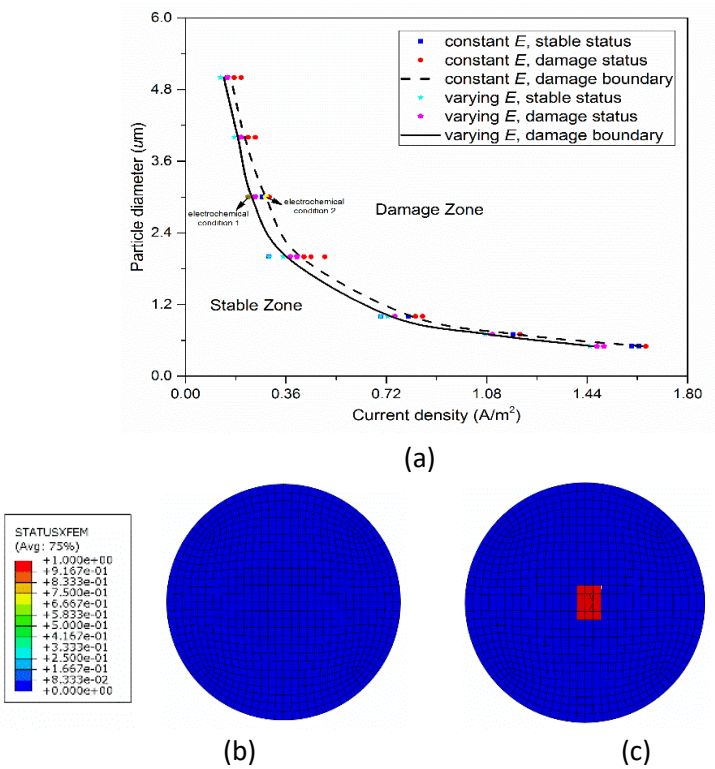

Fig 8. (a) Crack initiation boundary for 3*u*m diameter NCM primary particle considering concentration-dependent Young's modulus and constant average Young's modulus, crack and damage distribution with concentration-dependent Young's modulus under (b) 0.225A/m^2 (c) 0.2875A/m^2

3.2.2. Crack propagation

After the maximum principle stress within enriched element exceeding the damage initiation stress, the crack will gradually propagate in the element to the moment when the critical fracture energy is reached and the corresponding element is exposed to complete fracture. With the proceeding of intercalation-deintercalation process, more cohesive elements present fracture phenomenon which results in the overall mechanical destruction of the particle. Here, we conduct the crack propagation analysis with using 0.11J/m^2 as critical fracture energy [9] and figure out the integrated failure boundary for NCM primary particle in Fig 9. In Fig 9 (a), crack initiation boundary and particle fracture boundary divide the entire failure diagram to three zones, which are named as fracture zone, crack propagation zone and stable zone respectively. The following equations are fitted to acquire the corresponding particle dimension with respect to crack initiation (d_i) and fracture (d_f) status under given current density.

$$d_i = 0.7424 i_n^{-0.978} \quad \text{(crack initiation)} \tag{22-1}$$

$$d_f = 0.8155 i_n^{-0.979} \quad \text{(crack fracture)} \tag{22-2}$$

Where i_n denotes the applied current density.

What deserves to note is that, for bulky particle (diameter over 4um), the crack initiation boundary and fracture boundary are adjacent. It indicates that the bulky particle has brittle characteristic, and the crystal will be fracturing rapidly once crack initiates within crystal. The underlying reason for this phenomenon is that, the isometrical increment of current density will produce greater increment of stress for bulky particle comparing with small particle. Fig 9 (b) exhibits the variation of maximum principle stress against current density for different particle dimension, where the slopes of curves show that the maximum principle stress increases faster with the increasing of current density for bulky particle. Hence, when the crack initiates in the bulky particle, the increasing of current density will lead to more drastic growth of maximum principle stress which further accelerates the fracture of bulky particle.

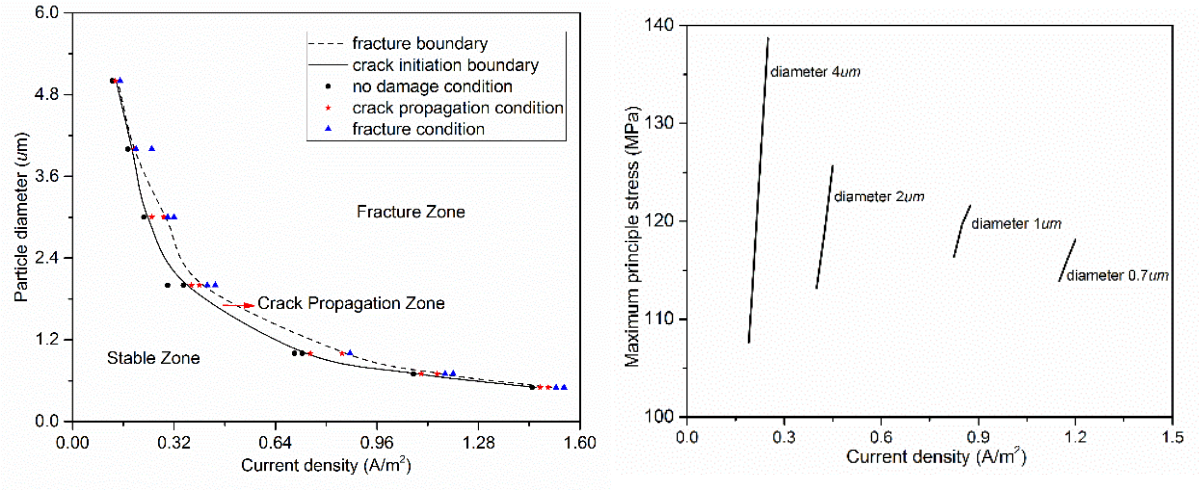

(a) (b)

Fig 9. (a) The Integrated fracture criteria diagram for NCM primary particle (b) the variation of maximum principle stress with current density for various particle dimensions

It is worth noting that, as the particles' size under micrometre scale are not uniform, there is a part of particles that will initiate crack or fracture under a specific current density, while the rest particles with relatively smaller dimension remain stable. Therefore, the connection between the

calculated critical particle dimension and the distribution of particle sizes in practical experiment samples is necessary to be established. We hereby introduce a concept of fracture proportion by associating the critical failure diagram with statistical analysis of microscopic particle size. For the certain electrochemical load, it is accessible to acquire the critical particle dimension for crack initiation and fracture with using the established Eq. (22-1), (22-2). Experimentally, we employ ImageJ software to measure and calculate the size distribution of NCM particles in the scanning electron microscopy (SEM) image as shown in Fig 10 (a), which is captured for a randomly selected area on NCM electrode before charging-discharging test. Fig 10 (b) plots the size distribution of NCM particles from SEM image. It is then available to obtain the fracture proportion that how many percentage of electrode particles initiate crack or fracture under specific current density. For electrode under 0.5A/m^2 current density, 22.22% particles represent cracking behaviour, among which 20.98% particles completely fracture.

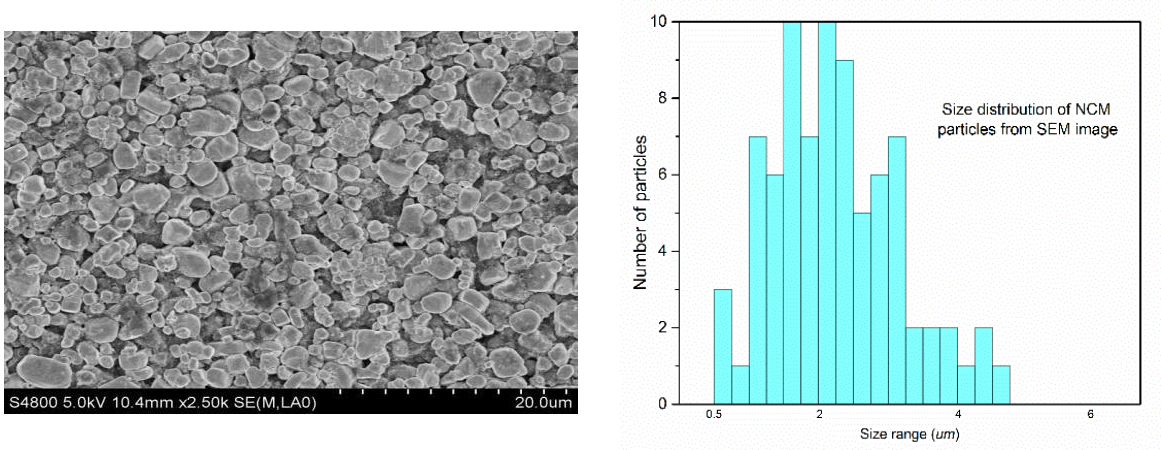

(a) (b)

Fig 10 (a) Scanning electron microscopy (SEM) image for a randomly selected area on NCM electrode before charging-discharging test, (b) size distribution of NCM particles from SEM image

Fig 11, 12 give the contours of crack initiation and evolution process for 3*um* particle experiencing 0.37A/m^2 current density during lithiation and delithiation phases respectively. We can observe that, for lithiation phase, crack initiates at the core of particle and gradually develops until 370s. At this moment, crack rapidly symmetrically propagates outward. Whereafter, crack slowly develops until the end of lithiation phase. This simulation result is in according with TXM tomogram [47], that microdefect of individual NCM particle initiates from the core of particle and propagates outward. In addition, at this lithiation phase, the crack has not penetrated the crystal and damage remains within the particle.

In Fig 12, two angles to observe the particle are collaterally exhibited to present the crack propagation at the particle inside and surface during delithiation phase. From which we can see that a new crack initiates on the particle surface at 204s, meanwhile the internal crack remains stable. The generation of surface crack can be explained from previous stress analysis that, during delithiation process, the maximum principle stress at outer surface zone keeps growing in tensile stress due to the concentration gradient change caused by Li-ion flow. Afterwards, this newly formed crack rapidly propagates at the particle surface accompanying with the extension of internal crack. The two cracks ultimately converge leading to the penetrative fracture of the particle, and the integral crack evolution process is so far given.

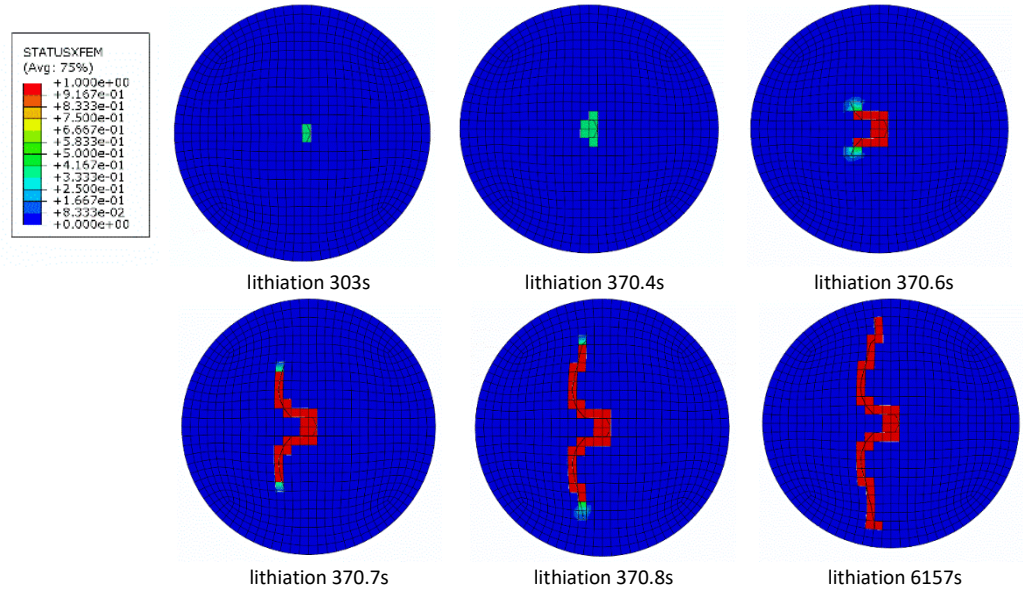

Fig 11. The continuous process of crack initiation and propagation under 0.37A/m^2 current density at lithiation phase

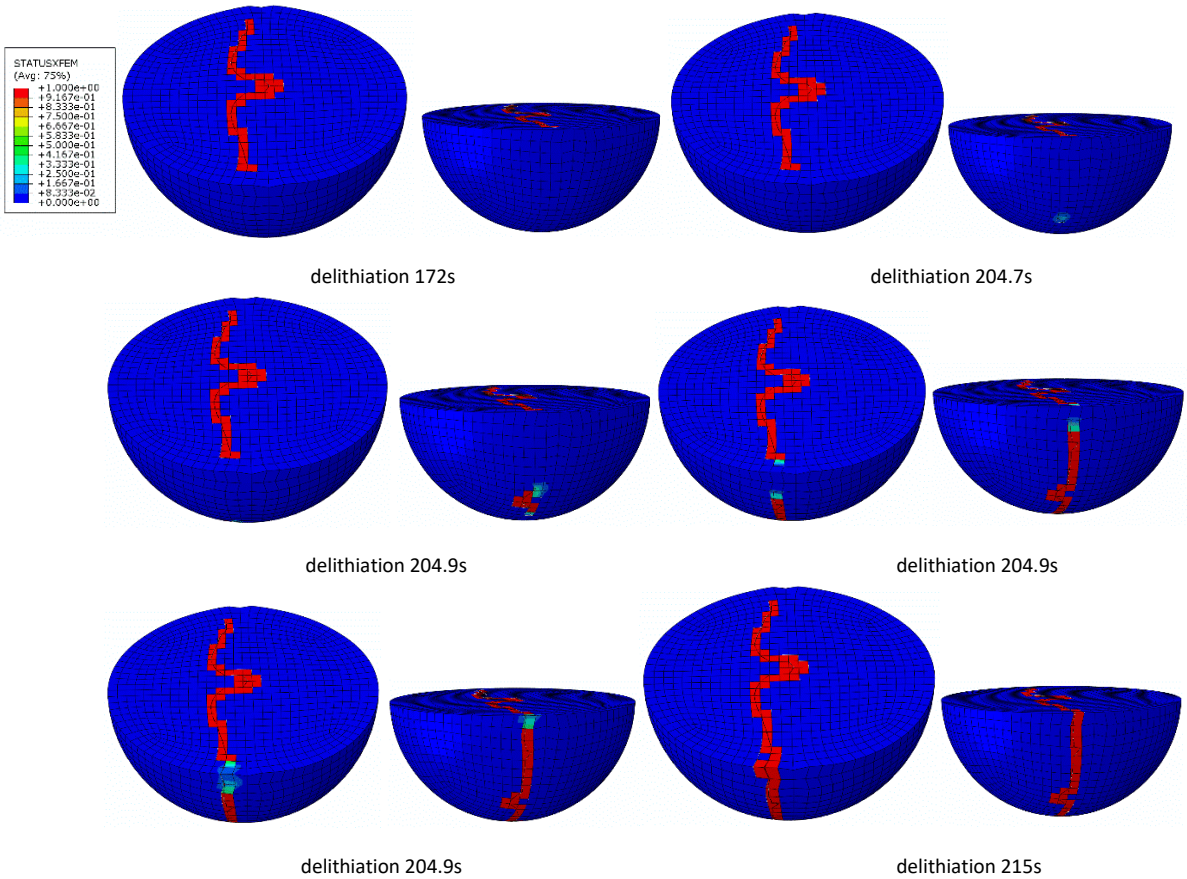

Fig 12. The continuous process of crack initiation and proprogation for 3*u*m diameter crystal under 0.37A/m^2 current density at delithiation phase

4. Conclusions

In this work, we have implemented the diffusion driven approach and chemical potential driven approach by developing ABAQUS user subroutines to perform the coupled diffusion-stress analyses of NCM primary particle, with considering the effect of diffusion on material property. Based on the

obtained diffusion-induced stress field, the integrated crack initiation, propagation and fracture evaluations have been comprehensively conducted by using the ABAQUS extended finite element method (XFEM). The critical failure diagram and semi-empirical equations have been established for avoiding the fracture phenomenon of primary electrode particle.

The comparison calculations show that, under the researched electrochemical conditions, two developed methods are accessible to generate almost the same diffusion-induced stress field and the diffusion-driven approach works with less computational consumption. Crack initiation and propagation analyses of NCM primary particle configuration are performed to avoid the rapid collapse. The research of mesh sensitivity is conducted to define the appropriate element size for cracking assessment. The integrated permissible diagram for crack initiation and fracture are established for estimating the cracking stages of primary particle under certain electrochemical load. It is worth noting that, the bulky particles (diameter over 4 *u*m) show brittle characteristics that the permissible electrochemical load of fracture is almost identical with that of crack initiation. The semi-empirical equations to calculate the critical particle dimension for crack initiation and fracture under given electrochemical loads are fitted. By combing the critical failure diagram with size distribution of electrode particles under microscale, it is accessible to define the fracture proportion that how many percentage of particles initiate crack or fracture under specific electrochemical condition. From the contour plots of typical crack onset and growth procedure, we can observe that the crack initiates at the core of particle and symmetrically propagates outward during lithiation phase. In delithiation phase, the internal crack gradually penetrates the particle accompanying with the formation of new surface crack. The aforementioned integrated crack evolution assessment provides a comprehensive understanding of the failure mechanism on primary particle experiencing diffusion induced stress.

Acknowledgments

The authors gratefully acknowledge the supports from the China Scholarship Council, Shanghai Automobile Industry Science and Technology Development Foundation (1801), National Natural Science Foundation of China (51828501), the Higher Education Discipline Innovation Project (111 Project) under the funding code B13020, University of Strathclyde and East China University of Science and Technology during the course of this work.

References

[1] B. Scrosati. Recent advances in lithium ion battery materials. Electrochimica Acta, 2000, 45(15-16):2461-2466.

[2] M. Armand, J.M. Tarascon. Building bettery batteries. Nature, 2008, 451(7179):652-657.

[3] J.W. Fergus. Recent developments in cathode materials for lithium ion batteries. Journal of Power Sources, 2010, 195(4):939-954.

[4] S. Amiri, X. Chen, A. Manes, M. Giglio. Investigation of the mechanical behavior of lithium-ion batteries by an indentation technique. International Journal of Mechanical Sciences, 2016, 105:1-10

[5] N. Nitta, F. Wu, J. T. Lee, G Yushin. Li-ion battery materials: present and future. Materials Today, 2015, 18:5.

[6] F. Schipper, E. M. Erickson, C. Erk, J.-Y. Shin, F. F. Chesneau, and D. Aurbach. Review—Recent Advances and Remaining Challenges for Lithium Ion Battery Cathodes. Journal of The Electrochemical Society, 2017, 164(1), A6220-A6228.

[7] J. A. Gilbert, J. Bareño, T. Spila, S. E. Trask, D. J. Miller, B. J. Polzin, A. N. Jansen, D. P. Abraham. Cycling Behavior of NCM523/Graphite Lithium-Ion Cells in the 3–4.4 V Range: Diagnostic Studies of Full Cells and Harvested Electrodes. Journal of The Electrochemical Society, 2017, 164(1): A6054-A6065.

[8] G.Y. Li, Z.J. Zhang, Z.L. Huang, C.K. Yang, Z.C. Zuo, H.H. Zhou. Understanding the accumulated cycle capacity fade caused by the secondary particle fracture of $LiNi_{1-x-y}Co_xMn_yO_2$ cathode for lithium ion batteries. Journal of Solid State Electrochemistry, 2017, 21(3), 673-682.

[9] R. Xu, L.S. de Vasconcelos, J. Shi, J. Li, K. Zhao. Disintegration of meatball electrodes for $LiNi_xMn_yCo_zO2$ cathode materials. Experimental Mechanics, 2018, 58, 549-559.

[10] Y. Zhang, C. Zhao, Z. Guo. Simulation of crack behavior of secondary particles in Li-ion battery electrodes during lithiation/ delithiation cycles. International Journal of Mechanical Sciences, 2019, 155:178-186

[11] P.F. Yan, J.M. Zheng, M. Gu, J. Xiao, J.G. Zhang, C.M. Wang. Intragranular cracking as a critical barrier for high-voltage usage of layer-structured cathode for lithium-ion batteries. Nature Communications, 2017, 8:14101.

[12] A. Mukhopadhyay, B.W. Sheldon. Deformation and stress in electrode materials for Li-ion batteries. Progress in Materials Science, 2014, 63, 58-116.

[13] L. Weng, J. Zhou, R. Cai. Analytical model of Li-ion diffusion-induced stress in nanowire and negative Poisson's ratio electrode under different operations. International Journal of Mechanical Sciences, 2018, 141:245-261.

[14] S. Prussin. Generation and Distribution of Dislocations by Solute Diffusion. Journal of Applied Physics, 1961, 32:1876.

[15] J.C.M. Li. Physical chemistry of some microstructural phenomena. Metallurgical Materials Transactions A, 1978, 9:1353

[16] J. Christensen, J. Newman. Stress generation and fracture in lithium insertion materials. Journal of Solid State Electrochemistry, 2006, 10, 293.

[17] Y.T. Cheng, M.W. Verbrugge. Evolution of stress within a spherical insertion electrode particle under potentiostatic and galvanostatic operation. Journal of Power Sources, 2009, 190, 2: 453-460.

[18] A.M. Korsunsky, T. Sui, B. Song. Explicit formulae for the internal stress in spherical particles of active material within lithium ion battery cathodes during charging and discharging. Materials and Design, 2015, 69: 247-252.

[19] X.C. Zhang, W. Shyy, A.M. Sastry. Numerical simulation of intercalation-induced stress in Li-ion battery electrode particles. Journal of The Electrochemical Society, 2007, 154(10), A910-A916.

[20] S.L. Zhang. Chemomechanical modeling of lithiation-induced failure in high-volume-change electrode materials for lithium ion batteries. Computational Materials, 2017, 3:7

[21] S. Kalnaus, K. Rhodes, C. Daniel. A study of lithium ion intercalation induced fracture of silicon particles used as anode material in Li-ion battery. Journal of Power Sources, 2011, 196(19):8116-8124.

[22] Z. Cui, F. Gao, J. Qu. A finite deformation stress-dependent chemical potential and its applications to lithium ion batteries. Journal of the Mechanics and Physics of Solids, 2012, 60(7):1280-1295.

[23] R. Purkayastha, R. McMeeking. A parameter study of intercalation of lithium into storage particles in a lithium-ion battery. Computational Materials Science, 2013, 80:2-14.

[24] L.M. Wu, X.H. Xiao, Y.H. Wen, J. Zhang. Three-dimensional finite element study on stress generation in synchrotron X-ray tomography reconstructed nickel-manganese-cobalt based half cell. Journal of Power Sources, 2016, 336, 8-18.

[25] E Chason, B.W. Sheldon. Monitoring stress in thin films during processing. Surface Engineering, 2003, 19:387

[26] J.M. Rosolen, F. Decker. Stress in carbon film electrodes during Li electrochemical intercalation. Journal of The Electrochemical Society, 1996, 143, 2417-2421.

[27] C. Bae, A. Manandhar, P. Kiesel, A. Raghavan. Monitoring the strain evolution of lithium-ion battery electrodes using an optical fiber Bragg Grating sensor. Energy Technology, 2016, 4, 851-855.

[28] J. Wolfenstine. Critical grain size for microcracking during lithium insertion. Journal of Power Sources, 1999, 79(1):111-113

[29] K.E. Aifantis, J.P. Dempsey. Stable crack growth in nanostructured Li-batteries. Journal of Power Sources, 2005, 143:203-211.

[30] Y Hu, X Zhao, Z Suo. Averting cracks caused by insertion reaction in lithium–ion batteries. Journal of Materials Research, 2010, 25(06): 1007-1010.

[31] K. Zhao, M. Pharr, J.J. Vlassak, Z. Suo. Fracture of electrodes in lithium-ion batteries caused by fast charging. Journal of Applied Physics, 2010, 108(073517): 1-6.

[32] F. Yang. Insertion-induced breakage of materials. Journal of Applied Physics, 2010, 108: 1-5

[33] Y.-T. Cheng, M.W. Verbrugge. Application of Hasselman's crack propagation model to insertion electrodes. Electrochemical and Solid State Letters, 2010, 13: A128-A131

[34] W. Woodford, Y. Chiang, W. Carter. "Electrochemical Shock" of intercalation electrodes: A Fracture Mechanics Analysis. Journal of The Electrochemical Society, 2010, 157(10): A1052-A1059.

[35] M. Klinsmann, D. Rosato, M. Kamlah, R.M. McMeeking. Modeling crack growth during Li insertion in storage particles using a fracture phase field approach. Journal of the Mechanics and Physics of Solids, 2016, 92:313-344.

[36] M. Klinsmann, D. Rosato, M. Kamlah, R.M. McMeeking. Modeling crack growth during Li extraction in storage particles using a fracture phase field approach. Journal of the Electrochemical Society, 2016, 163:102-118.

[37] R. Grantab, V.B. Shenoy. Location- and orientation-dependent progressive crack propagation in cylindrical graphite electrode particles. Journal of The Electrochemical Society, 2011, 158(8):A948

[38] M. Zhu, J. Park, A.M. Sastry. Fracture analysis of the cathode in Li-ion batteries: a simulation study. Journal of The Electrochemical Society, 2012, 159(4): A492-A498.

[39] J. Crank. The Mathematics of Diffusion. Oxford University Press, UK, 1979.

[40] B. Pan, A. Asundi, H. Xie, J. Gao. Digital image correlation using iterative least squares and pointwise least squares for displacement field and strain field measurements. Optics and Lasers in Engineering, 2009, 47(7-8):865-874.

[41] H. Hibbitt, B. Karlsson, P. Sorensen. ABAQUS Theory Manual, Version 6.12. Pawtucket, Rhode Island, USA, 2012.

[42] T. Belytschko, T. Black. Elastic crack growth in finite elements with minimal remeshing. International Journal for Numerical Methods in Engineering, 1999, 45(5): 601-620.

[43] F. Stuparu, D.M. Constantinescu, D.A. Apostol, M. Sandu. A combined cohesive elements-XFEM approach for analysing crack propagation in bounded joints. The Journal of Adhesion, 2016, 92:535-552.

[44] R. Xu, H. Sun, L. Vasconcelos, K. Zhao. Mechanical and structural degradation of $LiNi_xMn_yCo_zO_2$ cathode in Li-ion Batteries: An Experimental study. Journal of Electrochemical Society, 2017, 164(13):A3333-A3341

[45] A. Verma, K. Smith, S. Santhanagopalan, D. Abraham. K. Yao, P. Mukherjee. Galvanostatic intermittent titration and performance based analysis of $LiNi_{0.5}Co_{0.2}Mn_{0.3}O_2$ cathode. Journal of The Electrochemical Society, 2017, 164(13):A3380-A3392

[46] O. Dolotko, A. Senyshyn, M.J. Muhlbauer, K. Nikolowski, H. Ehrenberg. Understanding structural changes in NMC Li-ion cells by in situ neutron diffraction. Journal of Power Sources, 2014, 255:197-203

[47] P. Tsai, B. Wen, M. Wolfman, M. Choe, M. S. Pan, L. Su, K. Thornton, J. Cabana, Y. Chiang. Single-particle measurements of electrochemical kinetics in NMC and NCA cathodes for Li-ion batteries. Energy and Environmental Science, 2018, 11, 860.